Thermionic current densities from first principles

Johannes Voss, Aleksandra Vojvodic, Sharon H. Chou, Roger T. Howe, Igor Bargatin et al.

Citation: J. Chem. Phys. **138**, 204701 (2013); doi: 10.1063/1.4805002
View online: http://dx.doi.org/10.1063/1.4805002
View Table of Contents: http://jcp.aip.org/resource/1/JCPSA6/v138/i20
Published by the American Institute of Physics.

Thermionic current densities from first principles

Johannes Voss,[1,2,a)] Aleksandra Vojvodic,[1,2] Sharon H. Chou,[3] Roger T. Howe,[3] Igor Bargatin,[4] and Frank Abild-Pedersen[2,b)]
[1]*Department of Chemical Engineering, Stanford University, Stanford, California 94305, USA*
[2]*SUNCAT Center for Interface Science and Catalysis, SLAC National Accelerator Laboratory, Menlo Park, California 94025, USA*
[3]*Department of Electrical Engineering, Stanford University, Stanford, California 94305, USA*
[4]*Department of Mechanical Engineering and Applied Mechanics, University of Pennsylvania, Philadelphia, Pennsylvania 19104, USA*

(Received 8 March 2013; accepted 30 April 2013; published online 22 May 2013)

We present a density functional theory-based method for calculating thermionic emission currents from a cathode into vacuum using a non-equilibrium Green's function approach. It does not require semi-classical approximations or crude simplifications of the electronic structure used in previous methods and thus provides quantitative predictions of thermionic emission for adsorbate-coated surfaces. The obtained results match well with experimental measurements of temperature-dependent current densities. Our approach can thus enable computational design of composite electrode materials. © *2013 AIP Publishing LLC*. [http://dx.doi.org/10.1063/1.4805002]

I. INTRODUCTION

The efficiency of hot cathodes can be increased by developing new materials with sufficient thermionic emission of electrons operating at lower temperatures. These cathodes are important for a growing range of applications, including electron guns (used, e.g., in electron microscopes), thermionic energy converters and the recently demonstrated photon-enhanced thermionic energy converters.[1] Computational prediction of thermionic current densities will greatly aid the design of new electrodes. However, first-principles modeling of tunneling amplitudes governing thermionic emission has proven elusive. This article presents a method for calculating these tunneling rates from first principles, which is able to treat structurally complex surfaces. Hence we can predict thermionic emission from composite or multi-layer electrodes, which can often yield higher current densities than relatively simple elemental surfaces.

The work function of a metal surface, i.e., the energy required to remove an electron at the Fermi level from the metal, can easily be extracted from potential energies obtained within density functional theory (DFT). The prediction of electronic emission currents, however, also requires knowledge about the scattering properties of the surface. Existing approaches to calculating thermionic or field emission are based on crude approximations in terms of semi-classical statistics and averaging the surface electronic structure to one dimension, which restricts the applicability to simple surfaces.[2–5] In the case of field emission, previous first-principles calculations have considered a jellium model to describe the reservoir of electrons and have also used an average 1D potential.[6] Huang *et al.*[7] employed matching of wave functions in 3D to calculate field emission, but the analytical approximation of the wave functions decaying into vacuum yields non-zero currents only for finite fields and thermionic currents cannot be calculated. Musho *et al.*[8] accounted for quantum statistics in thermionic emission via Green's functions, but relied on simple wave functions with an effective electron mass and the work function as free parameters.

The method presented here does not involve semi-classical approximations nor simplification of the electronic structure, and is thus able to predict thermionic current densities purely from first principles even for complex surface structures with adsorbates. The method uses a non-equilibrium Green's function (NEGF) approach based on DFT calculations,[9,10] where both the semi-infinite systems of the metallic lead and vacuum are accounted for via self-energies, thus overcoming the limitations of existing approaches outlined above.

II. THEORY

The NEGF approach (see Refs. 9 and 10 for an introduction) allows for a description of systems that are not in thermodynamic equilibrium, e.g., due to the presence of reservoirs held at different chemical potentials or temperatures, which we use here to model steady currents due to temperature differences. We consider the non-interacting Kohn-Sham states[11] obtained from DFT calculations as eigenstates of the separate subsystems (reservoirs and scattering region) in equilibrium. We also neglect other interactions such as electron-phonon scattering, only considering coherent transport. Of central importance is the retarded single-particle Green's function of the system

$$G^{\mathrm{R}}(E) = (E + i\eta - H)^{-1}, \tag{1}$$

where the infinitesimally small parameter $\eta = 0^+$ assures that G^{R} describes the response to perturbations in the past, and H is the Hamiltonian of the system. In the following we will

a)Electronic mail: vossj@stanford.edu
b)Electronic mail: abild@slac.stanford.edu

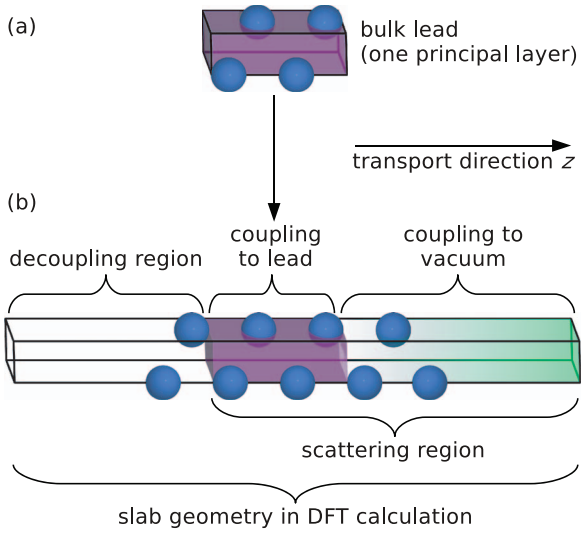

FIG. 1. Scheme of supercells employed in the DFT calculations using the example of W(110): bulk lead (a) and surface slab (b). W atoms are depicted by blue spheres. The purple (dark) volume corresponds to the metallic lead, the green (light) volume to the scattering region. The atoms in the unshaded part of the slab supercell serve as a decoupling region from the adjacent vacuum layer.

drop the superscript R from all Green's functions and self-energies, and we will also omit the term $i\eta$.

In NEGF transport calculations, the leads are typically modeled as semi-infinite systems,[9,10] serving as reservoirs for electrons and holes which are in thermodynamic equilibrium. To describe electronic emission through a surface into vacuum, we consider a semi-infinite metallic lead as a source and a semi-infinite vacuum region as a drain for electrons. The supercells employed to calculate the DFT bandstructures entering the Green's function calculations are depicted in Fig. 1 for bulk lead (a) and surface slab (b).

Approaches to treating the coupling of the scattering region to the semi-infinite reservoirs include matching of Kohn-Sham potentials with open boundary conditions on the scattering region[12] or extracting the coupling matrix elements by expansion of a DFT super cell Hamiltonian in a localized basis set.[13] We follow the latter approach, performing separate calculations for the scattering region (a surface slab) and for the periodically continued left- and right-hand sides of the system. The periodically continued systems are subdivided into principal layers along the transport direction.[14] These layers are chosen to be thick enough such that interactions beyond neighboring layers are negligible. Green's functions for principal layers of the isolated, semi-infinite systems are then calculated iteratively using a highly convergent scheme,[15] which relates the Green's function of a principal layer g_n ($n = 0$ is the surface layer) to that of the following principal layer g_{n+1} and vice versa via transfer matrices T and $\bar{T}$, respectively: $g_{n+1} = T g_n$ and $g_n = \bar{T}\, g_{n+1}$ for $n \to \infty$.

The interaction between the scattering region with both the lead and the vacuum is assumed to vanish beyond the adjacent principal layers, leading to a block-diagonal Hamiltonian,

$$H = \begin{pmatrix} H_\mathrm{L} & \tau_\mathrm{LS} & 0 \\ \tau_\mathrm{LS}^\dagger & H_\mathrm{S} & \tau_\mathrm{SV}^\dagger \\ 0 & \tau_\mathrm{SV} & H_\mathrm{V} \end{pmatrix}, \tag{2}$$

where the matrix blocks H_L, H_S, and H_V are the Hamiltonians of the bulk lead, scattering region, and vacuum region, respectively. τ_LS and τ_SV describe the interaction of the scattering region with the lead and with the vacuum, respectively. The Green's function of the scattering region G_S is then expressed using the Hamiltonian H_S and the self-energies Σ_L and Σ_V of the lead and the vacuum regions, respectively,[14]

$$G_\mathrm{S}(E) = [E - H_\mathrm{S} - \Sigma_\mathrm{L}(E) - \Sigma_\mathrm{V}(E)]^{-1}\,. \tag{3}$$

The self-energies are calculated from the lead and the vacuum surface principal layer Green's functions g_L and g_V, respectively,

$$\begin{aligned} \Sigma_\mathrm{L}(E) &= \tau_\mathrm{LS}^\dagger\, g_\mathrm{L}(E)\, \tau_\mathrm{LS}, \\ \Sigma_\mathrm{V}(E) &= (\tau_\mathrm{SV} - E\, S_\mathrm{V})^\dagger\, g_\mathrm{V}(E)\, (\tau_\mathrm{SV} - E\, S_\mathrm{V}), \end{aligned} \tag{4}$$

where S_V accounts for the overlap of the basis functions used for the slab and the vacuum region. This will be explained in detail below.

For the metallic lead, the calculation of the surface principal layer Green's function[15]

$$g_\mathrm{L}(E) = \left[E - h_\mathrm{L}^{00} - \left(h_\mathrm{L}^{01}\right)^\dagger \bar{T}_\mathrm{L}(E)\right]^{-1} \tag{5}$$

is based on the on-layer and layer-to-layer hopping matrices $h_\mathrm{L}^{00} = H_\mathrm{L}$ and h_L^{01}, respectively, represented here in a maximally-localized Wannier function (MLWF) basis[16,17] obtained from DFT calculations. $\bar{T}_\mathrm{L}$ is the lead transfer matrix. For all calculations presented here, we have chosen a principal layer thickness of four atomic layers for the metallic leads.

Since the momenta q_x, q_y perpendicular to the transport direction z are conserved, we only perform a Wannier transformation of the Bloch states $|\varepsilon^{\boldsymbol{q}}\rangle$ in the z-direction:

$$|w^{q_x,q_y,R_z}\rangle = \frac{c}{2\pi} \int \mathrm{d}q_z \sum_{\varepsilon^{\boldsymbol{q}}} U_{w\varepsilon}^{\boldsymbol{q}}\, \mathrm{e}^{-iq_z R_z} |\varepsilon^{\boldsymbol{q}}\rangle. \tag{6}$$

w enumerates the Wannier functions, U is a unitary matrix, c is the supercell lattice constant in the transport direction, and R_z is a lattice vector component. For the periodically continued vacuum system, the eigenstates are plane waves. We express the conserved in-plane components of the kinetic energy operator in momentum space, whereas the normal direction is described as a finite difference in real space (we use atomic units unless otherwise noted),

$$\begin{aligned} H_\mathrm{V} = {} & \frac{1}{2}\left(q_x^2 + q_y^2\right) \\ & + \frac{1}{2h^2}(2\delta_{z,z'} - \delta_{z,z'+1} - \delta_{z,z'-1})|z\rangle\langle z'| + \Phi, \end{aligned} \tag{7}$$

where z, z' denote vacuum sublayers along the transport direction. The addition of the work function Φ obtained from the surface slab calculation is required to align the subsystem

Hamiltonians in (2). For numerical convenience when evaluating τ_{SV} and S_V, the grid spacing h is chosen to match that of the Fourier grid used in the plane wave DFT calculation of the surface slab, i.e., the vacuum sublayer thickness h is of the order of 0.1 Å. The vacuum region in the slab, i.e. the principal vacuum surface layer, is thus spanned by the order of 100 sublayers. This is a good approximation, since states with energies too high to be sufficiently well represented in the basis determined by the chosen plane wave cut-off have a vanishing contribution to thermionic emission for the temperatures considered here. Considering the off-diagonal elements with $z \neq z'$ of (7) as coupling between neighboring principal vacuum layers through their outermost sublayers, the vacuum surface layer Green's function is calculated analogously to the above case of the metallic lead as

$$g_V(E) = \left[E - h_V^{00} - h_V^{01} T_V(E)\right]^{-1}. \tag{8}$$

h_V^{00}, h_V^{01}, and T_V are the on-layer, layer-to-layer hopping, and transfer matrices for the vacuum principal layers, respectively.

The interaction τ_{SV} between the scattering region and vacuum is calculated by projection of the scattering region Hamiltonian in its Wannier function representation onto the vacuum principal layer basis functions $|q_x, q_y, z\rangle$:

$$\langle q_x, q_y, z|\tau_{SV}|w^{q_x,q_y,R_z=0}\rangle = \langle q_x, q_y, z|\frac{c}{2\pi}\sum_{\varepsilon^{\boldsymbol{q}}} \varepsilon^{\boldsymbol{q}} U^{\boldsymbol{q}}_{w\varepsilon}|\varepsilon^{\boldsymbol{q}}\rangle. \tag{9}$$

Since the surface slab is aperiodic along z, there are no q-point sampling sub-divisions along z: $\boldsymbol{q} = (q_x, q_y, 0)$ and thus also $R_z = 0$. The Wannier functions extend into vacuum, and there is overlap with the vacuum basis functions $|q_x, q_y, z\rangle$:

$$\langle q_x, q_y, z|S_V|w^{q_x,q_y,R_z=0}\rangle = \langle q_x, q_y, z|w^{q_x,q_y,R_z=0}\rangle \neq 0. \tag{10}$$

The range of z considered in Eqs. (9) and (10) is restricted to be greater than some constant z_0, typically at a few Å above the surface. Note that the overlap matrix S_V partially compensates the effect of including small values of z into the calculation of τ_{SV}, such that the results for (3) are relatively insensitive to the exact choice of z_0.

Since z_0 lies relatively deep in the vacuum layer of the slab system, no ionic pseudo core spheres are included in the integration intervals. Therefore, all-electron and pseudo valence Bloch states coincide in the regions considered for integration, and no corrections due to ultrasoft pseudopotential or projector-augmented wave implementations in the DFT code appear.

We now consider the Landauer-Büttiker formalism,[18,19] in which the thermionic current density is given as

$$J(T) = \frac{1}{\pi A}\int \mathrm{d}E\, f[E - \mu(T), T]\, \mathcal{T}(E), \tag{11}$$

where A is the surface area of the considered supercell geometry, $f[E - \mu(T), T]$ is the Fermi-Dirac distribution, and

$$\mathcal{T}(E) = \mathrm{Tr}[\Gamma_L(E)\, G_S^{\dagger}(E)\, \Gamma_V(E)\, G_S(E)] \tag{12}$$

is the transmission function.[9,10] $\Gamma_{L/V}(E) = \mathrm{i}\,[\Sigma_{L/V}(E) - \Sigma_{L/V}^{\dagger}(E)]$ are broadening functions. Since q_x and q_y are good quantum numbers, $\mathcal{T}(E)$ can be calculated for fixed values of the in-plane momenta, where the total transmission is then given as a two-dimensional Brillouin zone integral.

We will compare first principles results obtained from (11) to experimental results, often available as fits against the Richardson-Dushman equation

$$J(T) = A\, T^2 \exp\left(-\frac{\Phi}{k_B T}\right). \tag{13}$$

This equation is based on a semi-classical treatment of an electron gas at a potential step.[3] A is the Richardson-Dushman constant, Φ is the work function, and k_B is Boltzmann's constant. Fitted constants of A and Φ effectively include first-order temperature dependencies of the work function and are, therefore, also referred to as the apparent Richardson-Dushman constant and work function, respectively.[3]

III. DETAILS OF CALCULATION

DFT calculations were performed with the DACAPO[20] ultrasoft pseudopotential[21] code. Kohn-Sham states were expanded in plane wave basis sets with a cutoff of 350 eV. Brillouin zones were sampled with k-point spacings of at most ~0.1 Å^{-1}. Fermi surface smearing was performed using Fermi-Dirac statistics with temperatures $k_B T \geq 0.1$ eV ($k_B T = 0.1$ eV was used for all structural relaxations, while higher temperatures were used to self-consistently calculate the temperature dependence of the work function; this temperature dependence can be more efficiently approximated by recalculating the Fermi level at different temperatures for fixed electronic energy levels). Transformation of Bloch states to Wannier functions was performed using the ASE software suite.[22]

IV. RESULTS

To compare results obtained using the presented first principles method to experimental findings, we consider the (100) and (110) surfaces of LaB_6 and W, respectively, as benchmark systems, since these surfaces are relatively stable and well-characterized at elevated temperatures.[23,24] We also consider W(110) surfaces with Cs adsorbates. Cs is known to lower the work function due to induced surface dipoles.[25] The influence of the adsorbates on electronic tunneling probabilities is an important physical effect which can be predicted with the presented method.

Both LaB_6 and tungsten exhibit very low thermal expansion coefficients of the order of a few 10^{-6} K^{-1}.[26,27] Assuming about 1% lattice constant expansion at high temperatures, the lattice expansion-induced work function changes are smaller than 0.05 eV, which we neglect here.

A. LaB_6(100)

Due to its thermal stability and low work function (2.3 eV for the most stable (100) surface), LaB_6 is commonly used as the cathode material for electron microscopes.[29] LaB_6 cleaves cleanly at (100) planes, leaving the surface terminated by La atoms.[23] DFT calculations using the Perdew-Burke-Ernzerhof[30] (PBE) exchange-correlation functional also yield

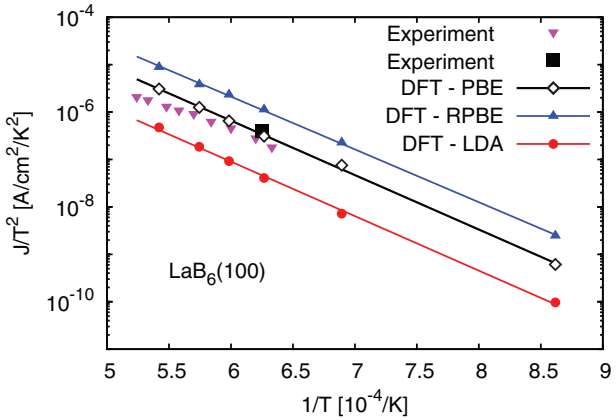

FIG. 2. Richardson-Dushman plot of thermionic emission from $LaB_6(100)$. Experimental data from Ref. 28 (▼) and Ref. 23 (■). The solid lines show fits of DFT results to Eq. (13) based on the PBE (◇), RPBE (▲), and LDA (●) exchange-correlation functionals, respectively.

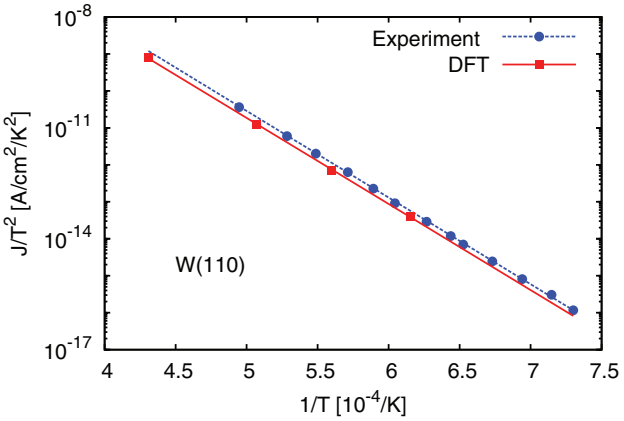

FIG. 3. Richardson-Dushman plot of thermionic emission from a close-packed tungsten surface with experimental data (●) from Ref. 24 and DFT results (■) based on the RPBE functional.

2.3 eV for the work function of the (100) surface,[31] while for the revised PBE[20] (RPBE) functional it is underestimated by 0.1 eV and for the local density approximation[11] (LDA) it is overestimated by 0.3 eV. Relaxing the surface structure according to the LDA functional increases the work function further by only 0.05 eV. We neglect the effect of different relaxed surface structures due to different functionals and focus on the dominant differences in the electronic structure only; all transport properties have been calculated for surfaces relaxed according to the PBE functional. Despite the fact that the LaB_6 work function is described best by the PBE functional, we also performed transport calculations using the LDA and RPBE functionals to benchmark the sensitivity of the emission current densities to the exchange-correlation functional employed.

Using the PBE approximation for the exchange and correlation functional also yields very good agreement with experiments[23,28] for thermionic current densities (Fig. 2), in particular for the current density reported in Ref. 23, where perfect stoichiometry and absence of reconstruction of the $LaB_6(100)$ surface was confirmed by Auger electron spectroscopy and low energy electron diffraction, respectively. In agreement with the trends in work functions described above, RPBE and LDA calculations over- and underestimate thermionic current densities of $LaB_6(100)$, respectively. Note that the apparent work functions obtained from fitting the DFT current density data to Eq. (13) differ less than the work functions listed above, which were obtained from the electrostatic potential for a fixed temperature ($k_BT = 0.1$ eV $\approx 1160\,\mathrm{K}\cdot k_B$). The apparent work functions for both PBE and LDA are about 2.3 eV, with 2.2 eV for RPBE.

B. W(110) and Cs/W(110)

For the tungsten surfaces, we employ the RPBE functional since it performs well for the description of covalent bonds to transition metal surfaces.[20] The bulk lattice constants of tungsten relaxed according to the PBE and RPBE functionals are very similar with values of 3.18 Å and 3.20 Å, respectively, in good agreement with the experimental result of 3.16 Å.[32] The fixed-temperature work function predicted using the RPBE functional is 4.61 eV for the W(110) surface (close to the experimental value of 4.65 eV),[24] while the PBE prediction is 0.14 eV higher. For an optimal description of the work function, we have chosen the RPBE functional also for the clean tungsten surface.

Current densities predicted from the presented method compare very well to experimental data[24] for the most stable W(110) surface (Fig. 3). The RPBE calculations yield a value of 4.62 eV and 4.61 eV for the apparent and fixed-temperature work functions at $k_BT = 0.1$ eV, respectively, comparing well to the experimental result for the apparent work function of 4.65 eV.[24]

Adsorbate-induced surface dipoles lower the work functions of the bare substrates. Here, we study cesiated tungsten as an example. We consider two coverage ratios of cesium atoms: one monolayer (ML), corresponding to about one Cs per 2×2 W(110) supercell, where the surface area per Cs is about the same as in Cs(110), and ∼0.69 ML (one Cs per 3×2 W(110) supercell), where the adsorbate-induced work function reduction is the largest.[33]

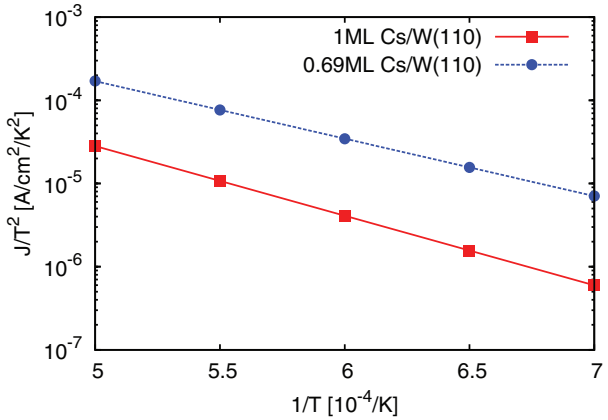

FIG. 4. Calculated thermionic current densities for cesiated W(110) based on the RPBE functional. The red (solid) line shows a fit of the DFT data to the Richardson-Dushman equation for monolayer Cs-coverage, the blue (dashed) line for (near optimal) 0.69 monolayer coverage.

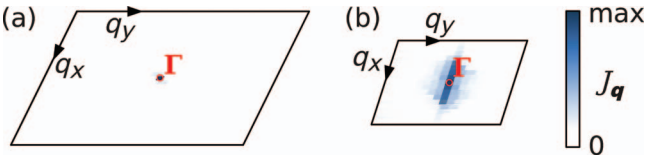

FIG. 5. Brillouin zone-resolved thermionic emission from clean (a) and cesiated (0.69 ML) W(110) (b) at $k_BT = 0.17$ eV obtained from RPBE calculations. The Brillouin zone of the cesiated system is smaller due to the 3×2 W(110) surface area.

Overall, the calculated thermionic current density at 0.69 ML coverage is higher than for 1 ML (Fig. 4), which is due to a lower work function of ∼1.4 eV for 0.69 ML compared to ∼1.6 eV at monolayer coverage. Experimental results yield $\Phi \approx 1.5$ eV and a Richardson-Dushman constant of $A \approx 3$ A/cm^2/K^2 for polycrystalline samples.[34] The DFT estimate for A is ∼0.5 A/cm^2/K^2. As the DFT results only represent the most stable tungsten surface, while the experimental results correspond to an average over orientations, the results cannot be compared quantitatively. However, a lower DFT estimate of A is plausible, considering that the DFT estimate of the work function at optimal coverage is 0.1 eV lower than the experimental one. This indicates that the DFT estimate of the adsorbate-induced surface dipole will be larger by a similar magnitude. Due to the opposite trends in current density with increasing magnitudes of Φ and A, the current densities estimated, e.g., at 1000 K from the experimental parameters and calculated within DFT only differ by a factor of about two.

The contribution of electrons with non-zero transverse momenta, $\boldsymbol{q}$, to the thermionic current densities for clean and cesiated W(110) (Fig. 5) shows that considering only the $\boldsymbol{q} = 0$ component of the current density is insufficient to describe thermionic emission from low-work function surfaces with adsorbates. For bare tungsten, an integral over the current density contributions at $k_BT = 0.17$ eV over ∼1% of the Brillouin zone around Γ accounts for ∼80% of the total current density. On the other hand, an integral over an equivalent area of the Brillouin zone of the cesiated system only yields ∼30% of the total current density. This shows that the description of thermionic emission of composite electrode surfaces with low work functions involving, e.g., adsorbates requires a three-dimensional description of the scattering problem.

V. CONCLUSION

We have developed a first-principles technique for calculating thermionic current densities which yields very good agreement with experiments. The method is based on non-equilibrium Green's functions. Unlike previous approaches, which involved semi-classical approximations or crude simplifications of the electronic structure, there are no limitations with respect to the complexity of materials for which current densities can be predicted with our method. This is particularly crucial for predicting the emission from complicated composite electrode materials including the important low-work function surfaces covered with alkali or alkali-earth adsorbates.

The predictive power of the method, which we have benchmarked against well-studied experimental systems, shows that this will be a very useful tool in the search for new cathode materials for future thermionic devices.

ACKNOWLEDGMENTS

Valuable discussions with Professor J. K. Nørskov and assistance from Dr. C. O'Grady are gratefully acknowledged. This work is supported by grants from the Global Climate and Energy Project (GCEP) at Stanford University, the U.S. Department of Energy under Contract No. DE-AC02-76SF00515 (F.A.P. and A.V.), and the National Science Foundation Graduate Research Fellowship Program (SHC).

[1] J. W. Schwede, I. Bargatin, D. C. Riley, B. E. Hardin, S. J. Rosenthal, Y. Sun, F. Schmitt, P. Pianetta, R. T. Howe, Z.-X. Shen, and N. A. Melosh, Nature Mater. **9**, 762 (2010).
[2] K. L. Jensen and M. Cahay, Appl. Phys. Lett. **88**, 154105 (2006); K. L. Jensen, J. Vac. Sci. Technol. B **21**, 1528 (2003); R. H. Fowler and L. Nordheim, Proc. R. Soc. London, Ser. A **119**, 173 (1928).
[3] C. Herring and M. H. Nichols, Rev. Mod. Phys. **21**, 185 (1949).
[4] A. Modinos, Surf. Sci. **115**, 469 (1982).
[5] R. Ramprasad, L. R. C. Fonseca, and P. von Allmen, Phys. Rev. B **62**, 5216 (2000).
[6] Y. Gohda, Y. Nakamura, K. Watanabe, and S. Watanabe, Phys. Rev. Lett. **85**, 1750 (2000).
[7] S. Huang, T. Leung, and C. Chan, Solid State Commun. **137**, 498 (2006).
[8] T. D. Musho, W. F. Paxton, J. L. Davidson, and D. G. Walker, J. Vac. Sci. Technol. B **31**, 021401 (2013).
[9] H. Haug and A.-P. Jauho, *Quantum Kinetics in Transport and Optics of Semiconductors*, 2nd ed. (Springer, Berlin, 2008).
[10] S. Datta, *Electronic Transport in Mesoscopic Systems* (Cambridge University Press, Cambridge, 1995).
[11] W. Kohn and L. J. Sham, Phys. Rev. **140**, A1133 (1965).
[12] J. Taylor, H. Guo, and J. Wang, Phys. Rev. B **63**, 245407 (2001).
[13] M. Brandbyge, J.-L. Mozos, P. Ordejón, J. Taylor, and K. Stokbro, Phys. Rev. B **65**, 165401 (2002).
[14] M. B. Nardelli, Phys. Rev. B **60**, 7828 (1999).
[15] M. P. Lopez Sancho, J. M. Lopez Sancho, and J. Rubio, J. Phys. F: Met. Phys. **14**, 1205 (1984); **15**, 851 (1985).
[16] N. Marzari and D. Vanderbilt, Phys. Rev. B **56**, 12847 (1997).
[17] K. S. Thygesen, L. B. Hansen, and K. W. Jacobsen, Phys. Rev. Lett. **94**, 026405 (2005).
[18] R. Landauer, IBM J. Res. Dev. **1**, 223 (1957); Philos. Mag. **21**, 863 (1970).
[19] M. Büttiker, Phys. Rev. B **33**, 3020 (1986).
[20] B. Hammer, L. B. Hansen, and J. K. Nørskov, Phys. Rev. B **59**, 7413 (1999).
[21] D. Vanderbilt, Phys. Rev. B **41**, 7892 (1990).
[22] S. R. Bahn and K. W. Jacobsen, Comput. Sci. Eng. **4**, 56 (2002).
[23] L. Swanson and D. McNeely, Surf. Sci. **83**, 11 (1979).
[24] M. H. Nichols, Phys. Rev. **57**, 297 (1940).
[25] V. Vlahos, J. H. Booske, and D. Morgan, Phys. Rev. B **81**, 054207 (2010).
[26] V. Craciun and D. Craciun, Appl. Surf. Sci. **247**, 384 (2005).
[27] F. C. Nix and D. MacNair, Phys. Rev. **61**, 74 (1942).
[28] M. Futamoto, M. Nakazawa, K. Usami, S. Hosoki, and U. Kawabe, J. Appl. Phys. **51**, 3869 (1980).
[29] R. Nishitani, M. Aono, T. Tanaka, C. Oshima, S. Kawai, H. Iwasaki, and S. Nakamura, Surf. Sci. **93**, 535 (1980).
[30] J. P. Perdew, K. Burke, and M. Ernzerhof, Phys. Rev. Lett. **77**, 3865 (1996).
[31] R. Monnier and B. Delley, Phys. Rev. B **70**, 193403 (2004).
[32] W. P. Davey, Phys. Rev. **26**, 736 (1925).
[33] S. H. Chou, J. Voss, I. Bargatin, A. Vojvodic, R. T. Howe, and F. Abild-Pedersen, J. Phys.: Condens. Matter **24**, 445007 (2012).
[34] D. Wright, in *Proceedings of the IEE—Part III: Radio and Communication Engineering* (IEE-Inst. Elec. Eng., Hertford, 1953), Vol. 100, p. 125.